1   # Lateral meltwater transfer across an Antarctic ice shelf

2

3   **Rebecca Dell[1,2], Neil Arnold[1], Ian Willis[1,3], Alison Banwell[3,1], Andrew Williamson[1],**

4   **and Hamish Pritchard[2]**

5

6   [1]Scott Polar Research Institute, Lensfield Road, Cambridge, CB2 1ER, UK

7   [2]British Antarctic Survey, High Cross, Madingley Road, Cambridge, CB3 0ET, UK

8   [3]Cooperative Institute for Research in Environmental Sciences, University of Colorado

9   Boulder, Boulder, CO, 80309, USA

10

11   *Correspondence to: Rebecca Dell (rld46@cam.ac.uk)*

12

13   ## Abstract

14

15   Surface meltwater on ice shelves can be stored as slush, in melt ponds, in surface streams
16   and rivers, and may also fill crevasses. The collapse of the Larsen B Ice Shelf in 2002 has
17   been attributed to the sudden drainage of ~3000 surface lakes, and has highlighted the
18   potential for surface water to cause ice shelf instability. Surface meltwater systems have
19   been identified across numerous Antarctic ice shelves, however, the extent to which these
20   systems impact ice shelf instability is poorly constrained. To better understand the role of
21   surface meltwater systems on ice shelves, it is important to track their seasonal
22   development, monitoring the fluctuations in surface water volume and the transfer of water
23   across the ice shelf. Here, we use Landsat 8 and Sentinel-2 imagery to track surface
24   meltwater across the Nivlisen Ice Shelf in the 2016-2017 melt season. Using the Fully
25   Automated Supraglacial-Water Tracking algorithm for Ice Shelves (FASTISh), we identify
26   and track the development of 1598 water bodies. The total volume of surface meltwater
27   peaks on 26th January 2017 at 5.5 x 10^7 m^3. 63 % of this total volume is held within two large
28   linear surface meltwater systems, which are orientated along the ice shelf's north-south axis
29   and appear to migrate away from the grounding line during the melt season, facilitating large
30   scale lateral water transfer towards the ice shelf front. This transfer is facilitated by two large
31   surface streams, which encompass smaller water bodies and follow the surface slope of the
32   ice shelf.

33

34   ## 1 Introduction

35

36   The total mass loss from Antarctica has increased from 40 ± 9 Gt/y in 1979–1990 to 252 ±
37   26 Gt/y in 2009–2017, providing a cumulative contribution to sea-level rise of 14.0 ± 2.0 mm
38   since 1979 (Rignot et al., 2019). Mass loss from Antarctica will likely increase in the near
39   future due, at least in part, to the shrinkage and thinning of some of its ice shelves (Siegert
40   et al 2019; DeConto and Pollard, 2016; Munneke et al., 2014) and the associated
41   acceleration of inland ice across the grounding lines (Fürst et al., 2016; Gundmundsson et
42   al., 2019). Seven out of 12 ice-shelves that bordered the Antarctic Peninsula have collapsed
43   in the last 50 years (Cook and Vaughan, 2010). One of the most notable events was the
44   February-March 2002 collapse of Larsen B, leading to both an instantaneous and longer-

45 term speedup of the glaciers previously buttressed by the ice shelf (Scambos et al., 2004;
46 Wuite et al., 2015; De Rydt et al., 2015), and resulting in their increased contribution to sea
47 level rise (Rignot et al., 2004).

48

49 The unforeseen catastrophic disintegration of Larsen B highlighted the unpredictable nature
50 of ice shelf collapse, and prompted a search for the causes of ice shelf instability. Current
51 understanding of the factors causing ice-shelf instability stems from the very limited number
52 of airborne and satellite observations prior to and following collapse events (e.g. Glasser
53 and Scambos, 2008; Scambos *et al.* 2009; Banwell et al., 2014), numerical modelling (e.g.
54 Vieli *et al.* 2006, Banwell *et al.* 2013, Banwell and MacAyeal, 2015), and the few in-situ
55 measurements investigating recent and current ice shelf processes (e.g. Hubbard *et al.*
56 2016; Banwell *et al.* 2019). It has been suggested that the chain reaction drainage of ~3000
57 surface meltwater lakes may have triggered the near-instantaneous break-up of Larsen B
58 (Robel and Banwell, 2019; Banwell et al., 2013), highlighting the potential importance of
59 surface hydrology for ice shelf instability.

60

61 Kingslake et al. (2017) identified numerous pervasive surface meltwater systems across
62 many of Antarctica's ice shelves. Meltwater production is often highest around grounding
63 lines, driven by high net shortwave radiation associated with low albedo blue ice areas, high
64 net longwave radiation around nunataks, and high sensible heat transfer from adiabatic
65 warming of katabatic winds (Bell et al., 2018; Lenaerts et al., 2017). Ice shelf hydrological
66 systems may then take several forms as meltwater may: (i) form surface streams and flow
67 downslope (e.g. Liston and Winther, 2005; Bell *et al.* 2017); (ii) collect in surface lakes (e.g.
68 Langley *et al.* 2016); (iii) percolate into the sub-surface and refreeze (Bevan et al., 2017;
69 Hubbard et al., 2016; Luckman et al., 2014); (iv) percolate into the subsurface and flow
70 laterally (Liston et al., 1999; Winther et al., 1996); or (v) percolate into the subsurface and
71 form sub-surface lakes and reservoirs (e.g. Lenaerts *et al.* 2017). Despite the identification
72 of pervasive meltwater systems, very little is known about their spatial and temporal
73 evolution, both within and between melt seasons. Furthermore, while surface water ponding
74 and the formation of lakes have been implicated in past ice shelf collapse events (Banwell
75 et al., 2013; Scambos et al., 2003), the formation of surface water streams that route water
76 quickly to the ice shelf front, may not necessarily cause instability but rather mitigate against
77 potential surface meltwater-driven collapse (Bell et al., 2017). Thus, whether future
78 projected increased surface melt on ice shelves forms lakes or flows rapidly to the ocean
79 via streams has important implications for future ice shelf stability and potential collapse
80 (Banwell, 2017; Bell et al., 2018). To better understand the role of these surface meltwater
81 features on ice-shelf instability, it is important to investigate the spatial and temporal
82 evolution of surface lakes and streams across entire ice shelves through entire summer melt
83 seasons.

84

85 In this paper, our objective is to develop a tool that can identify both surface lakes and
86 streams on Antarctic ice shelves and track their evolution over individual melt seasons. We
87 build on the work of Pope *et al.* (2016) and Selmes *et al.* (2011, 2013) and especially
88 Williamson *et al.* (2017; 2018a), who developed and used the FAST algorithm for tracking

89   lakes on the Greenland Ice Sheet (GrIS) using MODIS imagery. More specifically, we have
90   adapted the FASTER algorithm of Williamson, *et al.* (2018b) and Miles *et al.* (2017), who
91   adapted the FAST method to track GrIS lakes from the higher resolution Landsat-8 and
92   Sentinel-1 and -2 imagery. Here, we advance this later work to produce 'FASTISh', a Fully
93   Automated Supraglacial Lake and Stream Tracking Algorithm for Ice Shelves. We develop
94   the method for use with Landsat-8 and Sentinel-2 data to detect and differentiate between
95   surface lakes and streams and track them over time. We apply the technique to the Nivlisen
96   Ice Shelf, Antarctica, for the 2016-2017 melt season.
97
98   **2 Study Area**
99
100 The Nivlisen Ice Shelf (70.3 °S, 11.3°E), is situated in Dronning Maud Land, East Antarctica,
101 between the Vigrid and Lazarev ice shelves (Fig. 1). It has a surface area of 7,600 km², and
102 is 123 km wide by 92 km long. Ice thickness ranges from 150 m at the calving front to 700
103 m towards the southeast, and it exhibits flow velocities of around 100 m a^{-1} (Horwath et al.,
104 2006). To the southeast of the Nivlisen Ice Shelf, there is a bare ice region maintained by
105 katabatic winds, which extends in a south easterly direction for approximately 100 km
106 (Horwath et al., 2006). This bare ice region is characterised by ablation, and adjoins the
107 exposed bedrock nunatak (called the Shirmacheroasen), which is positioned where the ice
108 shelf meets the inland ice (Horwath et al., 2006). The ice shelf was selected for this study
109 as: i) pervasive surface meltwater features have previously been identified here in optical
110 satellite imagery (Kingslake et al., 2017); ii) meltwater features show changes over time
111 (Kingslake et al., 2015); and iii) the ice shelf is relatively small, allowing quick and efficient
112 development and application of FASTISh, before it may be used more widely across larger
113 Antarctic ice shelves.
114
115 **3 Methods**
116
117 There are three main components to the FASTISh algorithm: i) detecting lake and stream
118 areas; ii) calculating lake and stream depths and volumes; iii) tracking individual lakes and
119 streams and measuring their changing dimensions over time. These will be discussed in
120 sections 3.2 to 3.5 respectively, once the pre-processing steps applied to the imagery used
121 have been outlined (section 3.1).
122
123 **3.1 Images and Pre-Processing**
124
125 **3.1.1 Landsat 8**
126
127 Between 1st November 2016 and 30th April 2017, 12 Landsat 8 scenes with minimal cloud
128 cover, each partially covering the ice shelf extent, were identified and downloaded from the
129 USGS Earth Explorer website (https://earthexplorer.usgs.gov). Each scene was
130 downloaded as a Tier 2 data product, in the form of raw digital numbers (DN). Bands 2
131 (blue), 3 (green), 4 (red) and 8 (panchromatic) were used for this study (Fig. 2). Bands 2, 3,
132 and 4 have a 30 m spatial resolution, and Band 8 has a 15 m spatial resolution. Image scene

133 values were first converted from DN to Top-of-Atmosphere (TOA) values, to adjust for
134 variations in the per-pixel solar illumination angles. Each pixel was corrected for a specific
135 solar illumination angle based on metadata stored in the .ANG file, and following the 'Solar
136 and View Angle Generation Algorithm' suggested by NASA
137 (https://landsat.usgs.gov/sites/default/files/documents/LSDS-1928_L8-OLI-TIRS_Solar-
138 View-Angle-Generation_ADD.pdf). Converting from DN to TOA values on a per-pixel basis
139 is imperative when mosaicking and comparing images obtained at high latitudes.

140

141 For each Landsat scene, a cloud mask was generated using the 'Simple Cloud Score
142 Algorithm' (ee.Algorithms.Landsat.simpleCloudScore) in Google Earth Engine (GEE) and
143 then downloaded. The simple cloud score algorithm assigns a 'cloud score' to every pixel in
144 the image based on the following criteria: (i) brightness in bands 2 (blue), 3 (green), 4 (red);
145 (ii) brightness in just band 2 (blue); (iii) brightness in bands 5 (near infrared), 6 (shortwave
146 Infrared 1) and 7 (shortwave infrared 2); and iv) temperature in band 10 (thermal). The
147 algorithm also uses the Normalised Difference Snow Index (NDSI) to distinguish between
148 clouds and snow, which prevents snow from being incorrectly incorporated in the cloud
149 mask. The NDSI was developed by Hall *et al.* (2001) to distinguish between snow/ice and
150 cumulus clouds and is calculated from the following bands:

151

152 $$NDSI = (Blue - Near\ Infrared\ 1)/(Blue + Near\ Infrared\ 1) \qquad (1)$$

153

154 Prior to implementing the FASTISH algorithm, each Landsat scene and corresponding cloud
155 mask was clipped to the study area extent in ArcGIS using the batch clip process. This
156 process of clipping each scene to the same extent is required when comparing images
157 through the FASTISh algorithm. The 12 scenes formed six pairs, with two scenes per day
158 each covering part of the ice shelf, and so each scene pair was mosaicked using ArcGIS's
159 'mosaic to new raster' tool to produce six images. Thus, from Landsat imagery, we have
160 near-complete coverage of the ice shelf for six days of the 2016-2017 melt season (S.4). All
161 images were projected in the 1984 Stereographic South Pole co-ordinate system (EPSG:
162 3031).

163

164 **3.1.2 Sentinel-2**

165

166 20 Sentinel-2A level-1C scenes with minimal could cover were also downloaded between
167 1st November 2016 and 31st March 2017 from the Copernicus Hub web site
168 (https://scihub.copernicus.eu). Bands 2 (blue), 3 (green), 4 (red), and 11 (short wave infrared
169 (SWIR)) were then used. Bands 2, 3, and 4 had a spatial resolution of 10 m, and band 11
170 had a spatial resolution of 20 m. The Sentinel-2 data for all bands were downloaded as TOA
171 reflectance values, but needed to be divided by the 'quantification value' (found in the
172 metadata) of 10,000, to convert the numbers into values that lie within the expected zero to
173 one range. We applied this conversion to bands 2, 3 and 4, as these are the bands used to
174 identify water and calculate its depth, and their values need to be comparable to the values
175 provided by Landsat 8. Each downloaded scene was clipped, mosaicked to give images
176 with full coverage of the ice shelf, and then re-projected to the WGS 1984 Stereographic

177   South Pole co-ordinate system (EPSG: 3031), in line with the Landsat scenes (S.4). We
178   computed a cloud mask for each image using a thresholding approach, and pixels were
179   categorised as cloudy if the SWIR band value was > 10,000. This threshold was selected
180   through visually assessing the effectiveness of various thresholds against the corresponding
181   RGB scenes. As the resolution of the original SWIR band was 20 m, the resultant cloud
182   masks were resampled using nearest neighbor interpolation to 10 m spatial resolution. On
183   two image dates (14th November 2016 and 25th February 2017), this cloud masking
184   approach was not entirely successful, and additional individual masks were manually
185   created, to ensure all clouds were masked fully.
186
187   **3.2 Delineating Water Body Areas**
188
189   Lake and stream areas were determined using the Normalised Difference Water Index for
190   ice ($NDWI_{ice}$), which has widely been used previously to calculate the distribution of surface
191   meltwater features on the GrIS and on Antarctic ice shelves (e.g. Yang and Smith 2013;
192   Moussavi *et al.*, 2016; Koziol *et al.* 2017; Macdonald *et al.* 2018; Williamson *et al.* 2018b;
193   Banwell *et al.* 2019). It is calculated from the normalised ratio of the blue and red bands as:
194
195   $$NDWI_{ice} = (Blue - Red) / (Blue + Red) \qquad (2)$$
196
197   These bands were used because water has high reflectance values in the blue band, and
198   there is a relatively large contrast between ice and water in the red band (Yang and Smith,
199   2013). Studies typically apply a single $NDWI_{ice}$ threshold to an image, to classify pixels as
200   either 'wet' or 'dry' (e.g. Fitzpatrick et al., 2014; Moussavi *et al.* 2016; Miles *et al.* 2017). For
201   example, Banwell *et al.* (2019) applied a single threshold to distinguish water covered pixels
202   (>0.07) from ice pixels (≤0.07) on the McMurdo Ice Shelf, Antarctica. Across both Greenland
203   and Antarctica, most studies have used a relatively strict $NDWI_{ice}$ threshold of 0.25 to map
204   'deep' water bodies on ice (Yang and Smith 2013, Bell *et al.* 2017, Williamson *et al.* 2018b).
205   The same approach was applied to the Nivlisen Ice Shelf in this study in order to facilitate
206   the detection of deep water bodies only. This is important as if too much shallow water and
207   slush is detected, identifying and subsequently tracking individual water bodies over time
208   becomes difficult. Having applied a 0.25 $NDWI_{ice}$ threshold to the available images, each
209   resulting water mask was filtered using a two-dimensional connective threshold to remove
210   all groups of pixels of ≤ two pixels in Landsat 8 images and ≤ 18 pixels in Sentinel-2 images,
211   ensuring only water bodies with an area ≥ 1,800 m^2 were assessed further.
212
213   **3.3 Water Body Depth Calculations**
214
215   As discussed above, the $NDWI_{ice}$ method (Equation 2) is widely used for mapping water
216   body area, and has been used previously to provide qualitative assessments of water depths
217   across both Greenland and Antarctica. Quantitative calculations of water depth, however,
218   have favoured a different, more physically-based approach (Arnold et al., 2014; Banwell et
219   al., 2019, 2014; Pope, 2016; Pope et al., 2016; Sneed and Hamilton, 2007; Williamson et
220   al., 2017, 2018b), based on the original work of (Philpot, 1989), and this is the approach we

221   adopt in this study. Water depth, *z*, is calculated from:

222

223
$$z = \frac{[\ln(A_d - R_\infty) - \ln(R_{pix} - R_\infty)]}{g}$$
(3)

224

225   where R_{pix} is the satellite-measured pixel reflectance, A_d is the lake-bottom albedo, R_∞ is the
226   reflectance value for optically deep (> 40 m) water, and *g* is the coefficient associated with
227   the losses made during downward and upwards travel in a water column.

228

229   For the Landsat 8 images, water depths were calculated for each water pixel in each water
230   body using TOA reflectance data for both the red and panchromatic bands separately, and
231   then these values were averaged to give a single final value (Pope *et al.*, 2016; Williamson
232   *et al.*, 2018b). The average error associated with lake depths using this method has
233   previously been calculated to be zero, as the negative and positive errors cancel out (Pope
234   et al., 2016; Banwell et al., 2019). In our study, the panchromatic band was first resampled
235   using bilinear interpolation from 15 m to 30 m spatial resolution to match the resolution of
236   the red band. For the Sentinel-2 images, water body depths were calculated using the TOA
237   reflectance values in the red band only, as there is no equivalent panchromatic band
238   (Williamson *et al.* 2018b). To calculate A_d, the average reflectance value of the second
239   (Landsat) and sixth (Sentinel) ring of pixels surrounding each water body was calculated
240   (following a similar approach used by Arnold et al., 2014 and Banwell et al., 2014). The
241   second or sixth ring of pixels surrounding each lake was used to avoid calculating A_d from
242   slushy areas that border each water body; sixth-pixel rings were used for Sentinel-2 images
243   as these represent the same distance away from the water body as two-pixel rings in
244   Landsat images. Values for R_∞ were assessed on an image-by-image basis, by taking the
245   minimum reflectance value found over optically deep water (the ocean). For Landsat 8
246   imagery we used a *g* value of 0.7507 for the red band, and 0.3817 for the panchromatic
247   band (Pope *et al.*, 2016), and for Sentinel-2 imagery, we used a value of 0.8304 (Williamson
248   *et al.*, 2018b). Individual water body volumes were calculated by multiplying each pixel area
249   by its calculated water depth, and then summing across the water body. To facilitate
250   comparisons between Landsat 8 and Sentinel-2 data, area and depth arrays generated from
251   Landsat 8 images were then resampled to 10 m spatial resolution using nearest neighbour
252   interpolation.

253

254   **3.4 Classifying Water Body Types**

255

256   Having produced area and depth masks for each date, each identified water body was
257   categorised as either a lake or stream. This classification reflects only the morphology of
258   each water body, and does not imply anything about the rate of water flow. To distinguish
259   between lakes and streams we classified each water body based upon its solidity (defined
260   as the proportion of pixels of the water body that fall within its convex hull), which was
261   calculated using the 'regionprops' function in MATLAB. Water bodies with a solidity score ≥
262   0.45 were classified as individual lakes, and water bodies with a solidity score < 0.45 were
263   classified as streams. This threshold was selected by visually assessing the masks

264 generated from thresholds ranging between 0.42 and 0.49, in increments of 0.01, and
265 selecting the threshold that appears to best distinguish between more rounded lakes and
266 more linear streams.
267
268 **3.5 Tracking Water Bodies**
269
270 To track changes in the area and volume of surface meltwater bodies throughout the 2016-
271 2017 melt season, a maximum extent mask showing the maximum extent of all water bodies
272 during the melt season was generated by superimposing the areas of all water bodies
273 identified in each image (Williamson *et al.*, 2018b). The maximum extent mask was then
274 used to guide the tracking process, and each individual water body within the maximum
275 extent was prescribed an ID, and changes to the area and volume of each individual water
276 body over time were tracked within its maximum extent (Williamson *et al.*, 2018b).
277
278 In addition to tracking changes in the area and volume of each water body, the FASTISh
279 algorithm also tracks the water body type. To achieve this, a 3D matrix of all water bodies
280 was compiled, recording the area and volume of each water body over time, as well as
281 whether the water body is a lake or a stream. From this tracking process, four categories
282 were defined: (i) always a lake, (ii) always a stream, (iii) 'simple transitions' where a water
283 body is defined as *either* a lake or a stream and switches between the two categories (either
284 once or more than once, and in either direction), and (iv) 'envelopment transitions' where
285 water bodies spread and merge with neighbouring lakes and streams to form new, larger
286 bodies, or where larger bodies split into smaller lakes and streams. This final category allows
287 us to track the development of large surface water bodies across the ice shelf surface as it
288 identifies smaller water bodies being subsumed by larger water bodies as the melt season
289 progresses.
290
291 *3.5.1 Tracking volume loss from surface lakes*
292
293 Following previous studies (e.g. Fitzpatrick et al., 2014; Miles et al., 2017; Williamson et al.,
294 2018b), we identified and track volume losses from each water body in the 'always a lake'
295 category to better understand the local loss of surface melt water in seemingly isolated and
296 stationary water bodies. Previous studies have attempted to identify rapid drainage events,
297 defined as events where lakes lose > 80 % of their maximum volume in ≤ four days (e.g.
298 Fitzpatrick et al., 2014; Miles et al., 2017; Williamson et al., 2018b), however, the temporal
299 resolution of available imagery for the Nivlisen Ice Shelf is not great enough to facilitate this.
300 Therefore, we used our calculated volume time series to identify any lakes that lost > 80 %
301 of their maximum volume over the full melt season (referred to as 'loss events' hereafter).
302
303 **3.8 Digital Elevation Model**
304
305 To aid interpretations of the tracking results produced by the FASTISh algorithm, we used
306 surface elevation data from the REMA database (Howat et al., 2019). Figure 3a shows a
307 mosaic DEM product at 8 m resolution, which was used to visualize the topography of the

308   ice shelf and to plot the elevation distribution of some of the main water bodies identified. In
309   addition, a single 2 m data strip acquired on 31st January 2016, was used to extract the
310   elevation profiles along some of these main water bodies.
311

312   **3.7 Meteorological Data**

313

314   To put the calculations of meltwater volume into the context of seasonal variations in surface
315   meltwater production rates, we used surface air temperature and ground surface
316   temperature data for Novolazarevskaya station (70°46'04" S and 11°49'54"E), Nivlisen,
317   downloaded from the Russian Federation NADC, Arctic and Antarctic Research Institute
318   (AARI) (http://www.aari.aq). The station is positioned on the southeastern edge of the
319   Shirmacheroasen, and is 80 km inland from the Lazarev Sea Coast. Monthly mean averages
320   were plotted for the duration of the melt season (1 November 2016 - 30 April 2017).

321

322   **4 Results**

323

324   **4.1 Spatial Extent and Distribution of Surface Water Bodies**

325

326   The seasonal evolution of meltwater occurrence during the 2016-2017 summer is shown in
327   Figure 4. On 11th December 2016, few meltwater bodies exist, and they are predominantly
328   clustered towards the grounding line in the south-west, where the ice shelf surface is
329   relatively flat and the winter snow cover is thin (Fig. 4A). The majority of these water bodies
330   exist as distinct entities, and do not connect to one another. Some meltwater ponds are
331   identified in close proximity to the nunatak. The mean water depth on 11th December is 1.0
332   m, and the maximum water depth is 3.4 m.

333

334   By 17th December (Fig. 4B), there has been a marked increase in the area and volume of
335   surface meltwater, held in both surface lakes and streams; the mean water depth is 0.7 m
336   and the maximum water depth is 3.1 m. Several of the previously isolated ponds have
337   coalesced in some of the main topographic lows. The spatial extent of the surface water
338   bodies extends ~ 2 km further towards the ice shelf front. In addition, some water bodies
339   have begun to develop towards the eastern edge of the grounding line in a blue ice region.

340

341   By 27th December (Fig 4C), there is a marked development in the surface meltwater system,
342   as two surface streams have formed along the north-south axis (labelled a and b in Fig. 4C).
343   The Western stream (a) is ~ 6.5 km long and ~ 10 km from the Eastern stream (b), which is
344   ~ 8.5 km long and proximal to the surface lakes on the ice shelf's eastern margin. Overall,
345   there are fewer isolated lakes towards the grounding line, and the majority of the surface
346   meltwater is proximal to the two large surface streams, at elevations of ~ 60 m to 65 m (Fig.
347   3). The mean water depth of all identified water bodies is 0.9 m and the maximum water
348   depth is 4.7 m.

349

350   On 26th January 2017 (Fig. 4D), the area and volume of surface meltwater reaches a peak
351   for the summer, facilitated by the enlargement of the two large surface streams, which
352   involve the flooding of topographic lows, as water appears towards the firn further north on
353   the ice shelf. These streams are now (a) ~ 20.5 km and (b) ~ 16.9 km in length, and have a
354   mean depth of (a) 0.8 m and (b) 0.7 m. The mean depth of all water on 26th January 2017
355   is 0.6 m and the maximum water depth is 3.3 m.

356

357   On 13th February (Fig 4E), the two large streams remain prominent on the ice shelf, however
358   they have lost area, depth and volume at their southern ends. The mean water depth of all
359   water is 0.6 m and the maximum water depth is 4.3 m.
360
361   **4.2 Tracking Results**
362
363   Of the 1598 water bodies identified and tracked within the maximum extent matrix, 1458
364   (91%) are defined as always a lake, 42 (3%) are identified as always a stream, 51(3%) are
365   defined as simple transitions, and 47 (3%) are categorised as envelopment transitions.
366   Water bodies that are always a lake are predominantly clustered further south on the ice
367   shelf towards the grounding line, while water bodies defined as envelopment transitions are
368   found further north, towards the ice shelf front (Fig. 5).
369
370   *4.2.1 Total Area and Volume of Tracked Surface Water Bodies*
371
372   For each of the tracked water body categories, Table 1 shows the maximum area and
373   volume, and the corresponding dates on which these maxima were reached. The minimum
374   area and volume for all tracked categories is zero on 14th November 2016, as no deep
375   surface melt water was detected on that date. Although 91% of water bodies identified are
376   classified as lakes, lakes do not dominate the total area or volume of surface meltwater
377   (Table 1, Fig. 6). Conversely, the envelopment transitions, of which there are only 47 in total,
378   peak at 8.0 x 10^7 m^2 in area and 4.5 x 10^7 m^3 in volume on 26th January 2017, which is over
379   a month later than the peaks in area and volume recorded for the other three categories.
380   These envelopment transitions dominate the total area and volume signals for 'all water
381   bodies' (Table 1), which also reach their maxima on 26th January (Table 1, Fig. 6).
382
383   *4.2.2 Tracking Individual Water Bodies*
384
385   In addition to producing a time series of total surface water area and volume for each of the
386   four water body categories, the FASTISh tracking algorithm also produces time series of
387   individual water body areas and volumes. Over the 2016-2017 melt season, the two largest
388   envelopment transitions, referred to as the Western System (WS) and the Eastern System
389   (ES) hereafter (Fig. 5), propagate towards the ice shelf front as the melt season progresses,
390   and contain 62.6 % of the total surface water volume on 26th January 2017.
391
392   The volume of meltwater within the WS increases from zero on 11th December 2016 to a
393   maximum of 2.5 x 10^7 m^3 on 26th January 2017, before declining to zero again by 24th March
394   2017 (Fig. 7). The ES has a shorter lifespan, and is active between 27th December 2016
395   and 25th February 2017 (Fig. 7). Its volume peaks at 9.6 x 10^6 km^3 on the 26th January 2017
396   (Fig. 7). In line with the trends described in section 4.1, both the ES and WS migrate north
397   towards the ice shelf front as the melt season progresses.
398
399   Figure 7 shows the elevation distribution for each meltwater system on three dates: 27th
400   December 2016, 26th January 2017 and 13th February 2017. Overall, the WS occupies a
401   total elevation range of just 59 to 66 m (Fig. 7a). On 27th December 2016, the majority of
402   this surface water is held in the 62 to 63 m range, accounting for 5.4 x 10^6 m^2 (Fig. 7a). This
403   is also true at the height of the melt season, when 1.1 x 10^7 m^2 of water is within the 62 to
404   63 m bin on 26th January 2017. However, by 13th February 2017, the majority of the surface
405   water is held in the slightly lower 61 to 62 m elevation range, which accounts for 7.9 x 10^6
406   m^2 of surface melt (Fig. 7a). Over the three dates, the ES occupies a total elevation range

407 of 51 to 65 m (Fig. 7b). On 27th December 2016, the majority of the water (1.9 x 10^6 m^2) is
408 clustered at an elevation of 63 to 64 m, whilst on 26th January and 13th February 2017, 3.1
409 x 10^6 m^2 and 2.6 x 10^6 m^2 of water respectively is clustered within the 58 to 59 m bin.
410

411 Figure 8 shows the surface elevation profiles for the WS and the ES, which are extracted
412 from the maximum extent matrix (a composite image made by superimposing the areas of
413 all water bodies identified in each image, to retrieve the maximum extent of each water
414 body). Both systems are characterised by a downward sloping surface towards the ice shelf
415 front. The WS has a very shallow slope, with the elevation decreasing by ~ 2 m over the full
416 25.7 km profile (Fig. 8a), the ES is slightly steeper, showing a ~ 6 m decrease in elevation
417 over its full 27 km profile (Fig. 8b). While the overall trends for both profiles show a decrease
418 in elevation, both are also characterised by rhythmic variance and high frequency variability
419 over short distances (Fig. 8).
420

421 ### 4.2.2 Identifying Individual Lake Freeze Through/Drainage Events.
422

423 Figure 9 shows the loss in water volume through freeze-through or drainage for the 'always
424 a lake' category over the melt season, together with the ground surface temperatures and
425 surface air temperatures from the Novolazarevskaya Station. 805 lakes have a 'loss event'
426 by 27th December 2017, losing a total volume of 1.5 x 10^7 m^3, despite increasing air surface
427 and ground surface temperatures (Fig. 9).
428

429 ## 5 Discussion
430

431 ### Spatial and Temporal Distribution of Surface Meltwater Bodies
432

433 In the early melt season, surface meltwater on the Nivlisen Ice Shelf ponds in small surface
434 lakes that form in relatively flat areas towards the grounding line, in close proximity to the
435 Shirmacheroasen and blue ice regions (Figs. 3 and 4). This initial generation of surface
436 meltwater is likely driven by regional wind patterns and the effects of local ice-albedo, as the
437 relatively low albedo of the blue ice can lead to increased local melt rates (Bell et al., 2018;
438 Lenaerts et al., 2017; Stokes et al., 2019). Furthermore, areas of lower elevation towards
439 the grounding line are likely to be exposed to katabatic winds, which can result in near-
440 surface temperatures that are 3 K greater than temperatures further up-ice and down-ice
441 (Lenaerts *et al.* 2017). These persistent katabatic winds can also result in the production of
442 blue ice regions, as snow is eroded from the ice shelf surface (Lenaerts et al., 2017). Our
443 results for the early melt season on the Nivlisen Ice Shelf therefore support the findings of
444 Kingslake et al. (2017) who found, for a variety of ice shelves around Antarctica, that 50 %
445 of the ice shelf drainage systems are either within 8 km of rock exposures, or within 3.6 km
446 of blue ice surfaces.
447

448 Seasonal variations in the amount of surface meltwater on the Nivlisen Ice Shelf are driven
449 by weather, with increases in surface water area and volume corresponding with rising
450 ground and air surface temperatures (Fig. 9). However, as the melt season progresses,
451 there is a transition to a connected surface drainage network, which facilitates a progressive
452 transfer of surface meltwater away from the grounding line towards the ice shelf front. As
453 temperatures rise and surface water bodies increase in area and volume, they grow, merge
454 with nearby water bodies, and form new extended networks of surface lakes and streams
455 on the ice shelf surface. While rising ground and air temperatures are a strong control on

456 the amount of surface meltwater, the direction and extent of the identified lateral water
457 transfer is controlled by the ice shelf's surface topography (Fig. 3b). Over the course of the
458 melt season, the area and volume of surface meltwater decrease in the regions close to the
459 grounding line, and increase in more distal parts of the ice shelf.
460
461 The development of the two largest enveloping water bodies (WS and ES) dominate the
462 transition to a generally more connected drainage network. This is because these systems
463 facilitate large-scale transfer of water across the shelf, as water flows along linear
464 depressions from high to low elevations (Figs. 8 and 9). The ES and WS appear to be fed
465 by smaller surface lakes and streams, both above and below the grounding line, and as the
466 area and volume of the ES and WS increases, they spread and envelope nearby water
467 bodies, likely as water ponds up and flows over impermeable ice, which is refrozen surface
468 or shallow subsurface meltwater from previous years. Such processes were also observed
469 by Kingslake et al. (2015). The 'pulse' forward of the ES and WS between 27th December
470 2016 and 26th January 2017 does not appear to be controlled by a topographic 'lip' or 'dam',
471 and is therefore more likely to be the result of increased meltwater production, resulting in
472 saturation of the surrounding firn pack, which may bring it up to isothermal conditions,
473 thereby facilitating further melt and lateral transfer. By 26th January 2017, the ES and WS
474 are the dominant features within the entire Nivlisen Ice Shelf meltwater system, holding
475 62.6% of the surface meltwater volume. On this date, the ES and WS reach a length of ∼
476 16.9 km and ∼ 20.5 km respectively, although unlike observations on the Nansen Ice Shelf
477 (Bell et al., 2017), they do not facilitate the export of surface meltwater off the ice shelf front
478 via a waterfall. Instead, both systems always terminate at least ∼ 35 – 55 km from the ice
479 shelf front, suggesting that the water percolates into the surrounding firn in that area of the
480 ice shelf. Whilst the drainage system currently observed on the Nivlisen Ice Shelf does not
481 transfer surface meltwater all the way to the ice shelf front, it is plausible that such a system
482 will develop in the future, as the quantity of surface meltwater produced increases. Whilst
483 the water may pond, (possibly resulting in eventual hydrofracture and ice shelf collapse),
484 the ES and WS may also evolve quickly and sufficiently to allow water to flow off the ice
485 shelf front, effectively exporting the excess meltwater and mitigating some of the threats to
486 the ice shelf stability (Bell et al., 2017; Banwell, 2017).
487
488 Overall, 1.6 % of the Nivlisen Ice Shelf is occupied by a surface meltwater body at some
489 point during the 2016-2017 melt season, and over those areas, the mean water depth is
490 0.85 m. Comparatively, prior to its collapse, 5.3 % the Larsen B Ice Shelf was covered by a
491 surface meltwater body, and the mean water depth was 0.82 m (Banwell et al., 2014). Whilst
492 the mean water body depths between the Larsen B and Nivlisen Ice Shelves are
493 comparable, the spatial distributions of these water bodies, and the proportion of the ice
494 shelf that they cover, are different. Surface lakes were distributed relatively evenly across
495 the entire surface of Larsen B before it collapsed, whereas surface lakes are predominantly
496 clustered towards the grounding line on the Nivlisen Ice Shelf, and the transfer of surface
497 melt towards the ice shelf front and across snow/ firn covered regions is predominantly
498 facilitated by the WS and ES. The relatively extensive snow and firn cover on the Nivlisen
499 Ice Shelf likely prevents the development of a similar meltwater distribution to that observed
500 on the Larsen B Ice Shelf, as much of the surface meltwater is able to percolate into available
501 pore space.
502
503
504
505

Loss in Water Volume from Surface Lakes

The loss of 1.5×10^7 m³ of surface water from surface lakes by 27th December 2017, despite increasing air surface and ground surface temperatures (Fig. 9), coincides with an increase in the volume of water held within the enveloping water bodies, which continues to increase up to a maximum of 4.5×10^7 m³ on 26th January 2017. It is likely, therefore, that the loss of water from surface lakes at such an early stage in the melt season signifies the lateral transfer of water, away from the small 'isolated' lakes near the grounding line, and into the large enveloping water bodies, which hold and transport the surface meltwater across the ice shelf in more distal regions. This lateral transfer of water may be occurring through two mechanisms, (i) the over-topping of surface lakes, which results in the formation of shallow channels that connect water bodies and facilitate the transfer of water towards the ice shelf front (e.g. Banwell et al., 2019), or (ii) the gradual percolation of surface meltwater into the cold firn pack, which reduces the firn air content (FAC) of a region, therefore creating an impermeable surface over which water can flow (e.g. Kingslake et al., 2015). The firn may also become saturated enough to be isothermal, therefore melting and facilitating the flow of upstream ponded meltwater. This is particularly likely to occur near surface depressions such as those that are later occupied by the WS and ES. The FAC is determined by the melt to accumulation ratio, and if the surface melt on an ice shelf increases relative to precipitation, its FAC will drop, reducing the available pore space for meltwater storage (Lenaerts et al., 2017).

Potential Implications for Ice Shelf Stability

It is expected that the area of coverage and volume of surface meltwater on Antarctic ice shelves will increase into the future, in line with rising atmospheric temperatures (Bell et al., 2018; IPCC, 2019; Kingslake et al., 2017; Siegert et al., 2019). This surface water may have significant implications for ice shelf stability, as meltwater accumulation can lead to hydro-fracture, which could subsequently result in the collapse of an ice shelf, as seen on the Larsen B Ice Shelf in 2002 (Robel and Banwell, 2019; Banwell et al., 2013). An ice shelf may become increasingly vulnerable to hydrofracture if its FAC is reduced (Lenaerts et al., 2017). On ice shelves like the Nivlisen, where large scale lateral water transfer prevails, meltwater is delivered to locations that may otherwise not receive or experience much melt (Bell et al., 2017), and the FAC of these locations will, in turn, be reduced, increasing their susceptibility to surface meltwater ponding and hydrofracture. Surface meltwater re-freezing at the end of the melt season will also act as a significant source of heat, and the lateral transfer of surface melt could cause increased warming of the ice shelf and possible weakening in areas which currently do not experience significant summer melt. Were the maximum volume of surface meltwater we observe on the Nivlisen Ice Shelf in the 2016-2017 melt season (5.5×10^7 m³) to re-freeze over the maximum area of surface meltwater (9.1×10^7 m²), it would release an amount of energy equivalent to 49 days of potential solar energy receipts (Arnold and Rees, 2009), assuming an ice surface albedo of 0.86 (the mean value we observe over water-free distal areas of the ice shelf). Furthermore, large scale lateral water transfer and subsequent ponding may lead to ice shelf flexure (and therefore potential fracture) at locations that may have otherwise not been affected by flexure in response to meltwater loading (Banwell et al., 2013, 2019; Macayeal and Sergienko, 2013). However, evidence of lateral water transfer and export off the Nansen Ice Shelf has highlighted the potential for surface drainage systems to mitigate some of these meltwater driven instabilities (Bell et al., 2017).

6 Conclusions

We have adapted the pre-existing FASTER algorithm, developed for studying lakes on the GrIS (Williamson et al., 2018b), so that we can identify and track the area, depth and volume of both surface lakes and surface streams across Antarctic ice shelves. We refer to this new algorithm as FASTIsh, and have used it to study the changing spatial patterns of lakes and streams across the Nivlisen Ice Shelf in the 2016-2017 melt season. In total, we identify and track 1598 water bodies on the ice shelf over the course of the melt season. Surface water is initially generated towards the nunatak and blue ice region, in proximity to the grounding line. This region is relatively flat and has a low albedo, and we therefore observe localised ponding of surface meltwater. As the melt season progresses and air and ground surface temperatures increase, we see a transition from isolated localised ponding towards the grounding line to a more connected drainage system, that is influenced by the ice shelf topography. The middle of the melt season (e.g. 27th December 2016) is characterised by the progression of surface melt water bodies towards the thin snow band and firn-pack, as two large extensive drainage systems (the East System (ES) and West System (WS)) develop in long linear surface depressions. By the 26th January 2017, the ES and WS have fully developed, and facilitate the lateral transfer of surface melt up to 16.9 and 20.5 km north into the firn pack, and towards the ice shelf front. The transfer of surface meltwater to regions on the ice shelf that otherwise experience little surface melt may have implications for the structure and stability of the ice shelf in the future.

Code and Data Availability

The satellite imagery, REMA DEM, and meteorological data are all open access (see section 3). The MATLAB scripts used to process the data are available from the corresponding author upon request.

Author Contributions

RLD developed the methodology and scripts, building upon the prior work of AGW. NSA developed a script to convert Landsat DN values to per-pixel TOA values. RLD conducted the analysis and wrote the draft manuscript, under the supervision of all other authors. All authors discussed the results and were involved in editing of the manuscript.

Competing Interests

The authors declare no competing interests

Acknowledgements

The Cryosphere
Discussions
Open Access
EGU

609   **References**
610

611   Arnold, N. S., Banwell, A. F. and Willis, I. C.: High-resolution modelling of the seasonal
612   evolution of surface water storage on the Greenland Ice Sheet, Cryosph., 8(4), 1149–
613   1160, doi:10.5194/tc-8-1149-2014, 2014.
614   Arnold, N., & Rees, G. (2009). Effects of digital elevation model spatial resolution on
615   distributed calculations of solar radiation loading on a high arctic glacier. *Journal of
616   Glaciology*, *55*(194), 973–984. https://doi.org/10.3189/002214309790794959
617   Banwell, A.: Glaciology: Ice-shelf stability questioned, Nature, 544(7650), 306–307,
618   doi:10.1038/544306a, 2017.
619   Banwell, A. F., Willis, I. C., Macdonald, G. J., Goodsell, B. and MacAyeal, D. R.: Direct
620   measurements of ice-shelf flexure caused by surface meltwater ponding and drainage,
621   Nat. Commun., 10(1), doi:10.1038/s41467-019-08522-5, 2019.
622   Banwell, A. F. and MacAyeal, D. R.: Ice-shelf fracture due to viscoelastic flexure stress
623   induced by fill/drain cycles of supraglacial lakes, Antarct. Sci., 27(6), 587–597,
624   doi:10.1017/S0954102015000292, 2015.
625   Banwell, A. F., MacAyeal, D. R. and Sergienko, O. V.: Breakup of the Larsen B Ice Shelf
626   triggered by chain reaction drainage of supraglacial lakes, Geophys. Res. Lett., 40(22),
627   5872–5876, doi:10.1002/2013GL057694, 2013.
628   Banwell, A. F., Caballero, M., Arnold, N. S., Glasser, N. F., Cathles, L. Mac and MacAyeal,
629   D. R.: Supraglacial lakes on the Larsen B ice shelf, Antarctica, and at Paakitsoq, West
630   Greenland: A comparative study, Ann. Glaciol., 55(66), 1–8,
631   doi:10.3189/2014AoG66A049, 2014.
632   Bell, R. E., Chu, W., Kingslake, J., Das, I., Tedesco, M., Tinto, K. J., Zappa, C. J.,
633   Frezzotti, M., Boghosian, A. and Lee, W. S.: Antarctic ice shelf potentially stabilized by
634   export of meltwater in surface river, Nature, 544(7650), 344–348,
635   doi:10.1038/nature22048, 2017.
636   Bell, R. E., Banwell, A. F., Trusel, L. D. and Kingslake, J.: Antarctic surface hydrology and
637   impacts on ice-sheet mass balance, Nat. Clim. Chang., 8(12), 1044–1052,
638   doi:10.1038/s41558-018-0326-3, 2018.
639   Bevan, S. L., Luckman, A., Hubbard, B., Kulessa, B., Ashmore, D., Kuipers Munneke, P.,
640   O'Leary, M., Booth, A., Sevestre, H. and McGrath, D.: Centuries of intense surface melt on
641   Larsen C Ice Shelf, Cryosphere, 11(6), 2743–2753, doi:10.5194/tc-11-2743-2017, 2017.
642   Cook, A. J. and Vaughan, D. G.: Overviewing of areal changes of the ice shelves on the
643   Antarctic Peninsula over the past 50 years, Cryosph., 4, 77–98 [online] Available from:
644   http://dro.dur.ac.uk/20037/1/20037.pdf (Accessed 7 June 2018), 2010.
645   DeConto, R. M. and Pollard, D.: Contribution of Antarctica to past and future sea-level rise,
646   Nature, 531(7596), 591–597, doi:10.1038/nature17145, 2016.
647   Fitzpatrick, A. A. W., Hubbard, A. L., Box, J. E., Quincey, D. J., Van As, D., Mikkelsen, A.
648   P. B., Doyle, S. H., Dow, C. F., Hasholt, B. and Jones, G. A.: A decade (2002-2012) of

649 supraglacial lake volume estimates across Russell Glacier, West Greenland, Cryosphere,
650 8(1), 107–121, doi:10.5194/tc-8-107-2014, 2014.
651 Fürst, J. J., Durand, G., Gillet-Chaulet, F., Tavard, L., Rankl, M., Braun, M. and
652 Gagliardini, O.: The safety band of Antarctic ice shelves, Nat. Clim. Chang., 6(5), 479–482,
653 doi:10.1038/nclimate2912, 2016.
654 Glasser, N. F. and Scambos, T. A.: A structural glaciological analysis of the 2002 Larsen B
655 ice-shelf collapse, J. Glaciol., 54(184), 3–16, doi:10.3189/002214308784409017, 2008.
656 Gudmundsson, G. H., Paolo, F. S., Adusumilli, S. and Fricker, H. A.: Instantaneous
657 Antarctic ice-sheet mass loss driven by thinning ice shelves, Geophys. Res. Lett.,
658 2019GL085027, doi:10.1029/2019GL085027, 2019.
659 Hall, D. K., Branch, H. S., Tait, A. B., Riggs, G. A., Corporation, D. S., Salomonson, V. V,
660 Directorate, E. S., Chien, J. Y. L., Corporation, G. S. and Klein, A. G.: Algorithm
661 Theoretical Basis Document (ATBD) for the MODIS Snow-, Lake Ice- and Sea Ice-
662 Mapping Algorithms, Analysis [online] Available from:
663 https://eospso.gsfc.nasa.gov/sites/default/files/atbd/atbd_mod10.pdf (Accessed 21 April
664 2019), 2001.
665 Horwath, M., Dietrich, R., Baessler, M., Nixdorf, U., Steinhage, D., Fritzsche, D., Damm, V.
666 and Reitmayr, G.: Nivlisen, an Antarctic ice shelf in Dronning Maud Land: Geodetic-
667 glaciological results from a combined analysis of ice thickness, ice surface height and ice-
668 flow observations, J. Glaciol., 52(176), 17–30, doi:10.3189/172756506781828953, 2006.
669 Howat, I. M., Porter, C., Smith, B. E., Noh, M. J. and Morin, P.: The reference elevation
670 model of antarctica, Cryosphere, 13(2), 665–674, doi:10.5194/tc-13-665-2019, 2019.
671 Hubbard, B., Luckman, A., Ashmore, D. W., Bevan, S., Kulessa, B., Kuipers Munneke, P.,
672 Philippe, M., Jansen, D., Booth, A., Sevestre, H., Tison, J. L., O'Leary, M. and Rutt, I.:
673 Massive subsurface ice formed by refreezing of ice-shelf melt ponds, Nat. Commun., 7,
674 doi:10.1038/ncomms11897, 2016.
675 IPCC: Special Report on the Ocean and Cryosphere in a Changing Climate - Technical
676 Summary (Final Draft). [online] Available from: https://www.ipcc.ch/srocc/ (Accessed 18
677 December 2019), 2019.
678 Kingslake, J., Ng, F. and Sole, A.: Modelling channelized surface drainage of supraglacial
679 lakes, J. Glaciol., 61(225), 185–199, doi:10.3189/2015JoG14J158, 2015.
680 Kingslake, J., Ely, J. C., Das, I. and Bell, R. E.: Widespread movement of meltwater onto
681 and across Antarctic ice shelves, Nature, 544(7650), 349–352, doi:10.1038/nature22049,
682 2017.
683 Koziol, C., Arnold, N., Pope, A. and Colgan, W.: Quantifying supraglacial meltwater
684 pathways in the Paakitsoq region, West Greenland, J. Glaciol., 63(239), 464–476,
685 doi:10.1017/jog.2017.5, 2017.
686 Langley, E. S., Leeson, A. A., Stokes, C. R. and Jamieson, S. S. R.: Seasonal evolution of
687 supraglacial lakes on an East Antarctic outlet glacier, Geophys. Res. Lett., 43(16), 8563–
688 8571, doi:10.1002/2016GL069511, 2016.
689 Lenaerts, J., Lhermitte, S., Drews, R., Ligtenberg, S. R. M., Berger, S., Helm, V., Smeets,
690 P. C. J. P., van den Broeke, M. R., van De Berg, W. J., van Meijgaard, E., Eijkelboom, M.,
691 Eisen, O. and Pattyn, F.: Meltwater produced by wind – albedo interaction stored in an
692 East Antarctic ice shelf, Nat. Clim. Chang., 7, 58–63, doi:10.1038/NCLIMATE3180, 2017.
693 Liston, G. E. and Winther, J. G.: Antarctic surface and subsurface snow and ice melt
694 fluxes, J. Clim., 18(10), 1469–1481, doi:10.1175/JCLI3344.1, 2005.
695 Liston, G. E., Winther, J. G., Bruland, O., Elvehøy, H. and Sand, K.: Below-surface ice
696 melt on the coastal Antarctic ice sheet, J. Glaciol., 45(150), 273–285,
697 doi:10.3189/s0022143000001775, 1999.
698 Luckman, A., Elvidge, A., Jansen, D., Kulessa, B., Kuipers Munneke, P., King, J. and

15

The Cryosphere
Discussions

Open Access

EGU

699   Barrand, N. E.: Surface melt and ponding on Larsen C Ice Shelf and the impact of föhn
700   winds, Antarct. Sci., 26(6), 625–635, doi:10.1017/S0954102014000339, 2014.
701   Macayeal, D. R. and Sergienko, O. V.: The flexural dynamics of melting ice shelves, Ann.
702   Glaciol., 54(63), 1–10, doi:10.3189/2013AoG63A256, 2013.
703   Macdonald, G. J., Banwell, A. F. and Macayeal, D. R.: Seasonal evolution of supraglacial
704   lakes on a floating ice tongue , Petermann Glacier , Greenland, , 1–10,
705   doi:10.1017/aog.2018.9, 2018.
706   Miles, K. E., Willis, I. C., Benedek, C. L., Williamson, A. G. and Tedesco, M.: Toward
707   Monitoring Surface and Subsurface Lakes on the Greenland Ice Sheet Using Sentinel-1
708   SAR and Landsat-8 OLI Imagery, Front. Earth Sci., 5, doi:10.3389/feart.2017.00058, 2017.
709   Mouginot, J., Scheuchl, B. and Rignot., E.: MEaSUREs Antarctic Boundaries for IPY 2007-
710   2009 from Satellite Radar, Version 2., NASA Natl. Snow Ice Data Cent. Distrib. Act. Arch.
711   Center., doi:https://doi.org/10.5067/AXE4121732AD, 2017.
712   Moussavi, M. S., Abdalati, W., Pope, A., Scambos, T., Tedesco, M., MacFerrin, M. and
713   Grigsby, S.: Derivation and validation of supraglacial lake volumes on the Greenland Ice
714   Sheet from high-resolution satellite imagery, Remote Sens. Environ., 183, 294–303,
715   doi:10.1016/j.rse.2016.05.024, 2016.
716   Munneke, P. K., Ligtenberg, S. R. M., Van Den Broeke, M. R. and Vaughan, D. G.: Firn air
717   depletion as a precursor of Antarctic ice-shelf collapse, J. Glaciol., 60(220), 205–214,
718   doi:10.3189/2014JoG13J183, 2014.
719   Philpot, W. D.: Bathymetric mapping with passive multispectral imagery, Appl. Opt., 28(8),
720   1569, doi:10.1364/ao.28.001569, 1989.
721   Pope, A.: Reproducibly estimating and evaluating supraglacial lake depth with Landsat 8
722   and other multispectral sensors, Earth Sp. Sci., 3(4), 176–188,
723   doi:10.1002/2015EA000125, 2016.
724   Pope, A., Scambos, T. A., Moussavi, M., Tedesco, M., Willis, M., Shean, D. and Grigsby,
725   S.: Estimating supraglacial lake depth in West Greenland using Landsat 8 and comparison
726   with other multispectral methods, Cryosphere, 10(1), 15–27, doi:10.5194/tc-10-15-2016,
727   2016.
728   Rignot, E., Casassa, G., Gogineni, P., Krabill, W., Rivera, A. and Thomas, R.: Accelerated
729   ice discharge from the Antarctic Peninsula following the collapse of Larsen B ice shelf,
730   Geophys. Res. Lett., 31(18), L18401, doi:10.1029/2004GL020697, 2004.
731   Rignot, E., Mouginot, J., Scheuchl, B., Van Den Broeke, M., Van Wessem, M. J. and
732   Morlighem, M.: Four decades of Antarctic ice sheet mass balance from 1979–2017, Proc.
733   Natl. Acad. Sci. U. S. A., 116(4), 1095–1103, doi:10.1073/pnas.1812883116, 2019.
734   Robel, A. A. and Banwell, A. F.: A Speed Limit on Ice Shelf Collapse Through
735   Hydrofracture, Geophys. Res. Lett., 46(21), 12092–12100, doi:10.1029/2019GL084397,
736   2019.
737   De Rydt, J., Gudmundsson, G. H., Rott, H. and Bamber, J. L.: Modeling the instantaneous
738   response of glaciers after the collapse of the Larsen B Ice Shelf, Geophys. Res. Lett.,
739   42(13), 5355–5363, doi:10.1002/2015GL064355, 2015.
740   Scambos, T., Hulbe, C. and Fahnestock, M.: Climate-induced ice shelf disintegration in the
741   Antrctic Peninsula, in Antarctica Peninsula climate variability: a historical and paleo-
742   environmental perspective, pp. 79–92., 2003.
743   Scambos, T., Fricker, H. A., Liu, C. C., Bohlander, J., Fastook, J., Sargent, A., Massom, R.
744   and Wu, A. M.: Ice shelf disintegration by plate bending and hydro-fracture—Satellite
745   observations and model results of the 2008 Wilkins ice shelf break-ups, Earth Planet. Sci.
746   Lett., 280ID–6, 51–60, doi:10.1016/j.epsl.2008.12.027, 2009.
747   Scambos, T. A., Bohlander, J. A., Shuman, C. A. and Skvarca, P.: Glacier acceleration
748   and thinning after ice shelf collapse in the Larsen B embayment, Antarctica, Geophys.

749 Res. Lett., 31(18), L18402, doi:10.1029/2004GL020670, 2004.
750 Selmes, N., Murray, T. and James, T. D.: Fast draining lakes on the Greenland Ice Sheet,
751 Geophys. Res. Lett., 38(15), n/a-n/a, doi:10.1029/2011GL047872, 2011.
752 Selmes, N., Murray, T. and James, T. D.: Characterizing supraglacial lake drainage and
753 freezing on the Greenland Ice Sheet, Cryosph. Discuss., 7(1), 475–505, doi:10.5194/tcd-7-
754 475-2013, 2013.
755 Siegert, M., Atkinson, A., Banwell, A., Brandon, M., Convey, P., Davies, B., Downie, R.,
756 Edwards, T., Hubbard, B., Marshall, G., Rogelj, J., Rumble, J., Stroeve, J. and Vaughan,
757 D.: The Antarctic Peninsula under a 1.5°C global warming scenario, Front. Environ. Sci.,
758 7(JUN), doi:10.3389/fenvs.2019.00102, 2019.
759 Sneed, W. A. and Hamilton, G. S.: Evolution of melt pond volume on the surface of the
760 Greenland Ice Sheet, Geophys. Res. Lett., 34(3), L03501, doi:10.1029/2006GL028697,
761 2007.
762 Stokes, C. R., Sanderson, J. E., Miles, B. W. J., Jamieson, S. S. R. and Leeson, A. A.:
763 Widespread distribution of supraglacial lakes around the margin of the East Antarctic Ice
764 Sheet, Sci. Rep., 9(1), doi:10.1038/s41598-019-50343-5, 2019.
765 Tedesco, M., Lthje, M., Steffen, K., Steiner, N., Fettweis, X., Willis, I., Bayou, N. and
766 Banwell, A.: Measurement and modeling of ablation of the bottom of supraglacial lakes in
767 western Greenland, Geophys. Res. Lett., 39(2), n/a-n/a, doi:10.1029/2011GL049882,
768 2012.
769 Vieli, A., Payne, A. J., Du, Z. and Shepherd, A.: Numerical modelling and data assimilation
770 of the Larsen B ice shelf, Antarctic Peninsula, Philos. Trans. R. Soc. A Math. Phys. Eng.
771 Sci., 364(1844), 1815–1839, doi:10.1098/rsta.2006.1800, 2006.
772 Williamson, A. G., Arnold, N. S., Banwell, A. F. and Willis, I. C.: A Fully Automated
773 Supraglacial lake area and volume Tracking ("FAST") algorithm: Development and
774 application using MODIS imagery of West Greenland, Remote Sens. Environ., 196, 113–
775 133, doi:10.1016/j.rse.2017.04.032, 2017.
776 Williamson, A. G., Willis, I. C., Arnold, N. S. and Banwell, A. F.: Controls on rapid
777 supraglacial lake drainage in West Greenland: an Exploratory Data Analysis approach, J.
778 Glaciol., 1–19, doi:10.1017/jog.2018.8, 2018a.
779 Williamson, A. G., Banwell, A. F., Willis, I. C. and Arnold, N. S.: Dual-satellite (Sentinel-2
780 and Landsat 8) remote sensing of supraglacial lakes in Greenland, Cryosph., 12(9), 3045–
781 3065, doi:10.5194/tc-12-3045-2018, 2018b.
782 Winther, J.-G. G., Elvehøy, H., Bøggild, C. E., Sand, K. and Liston, G.: Melting, runoff and
783 the formation of frozen lakes in a mixed snow and blue-ice field in Dronning Maud Land,
784 Antarctica, J. Glaciol., 42(141), 271–278, doi:10.3189/s0022143000004135, 1996.
785 Wuite, J., Rott, H., Hetzenecker, M., Floricioiu, D., De Rydt, J., Gudmundsson, G. H.,
786 Nagler, T. and Kern, M.: Evolution of surface velocities and ice discharge of Larsen B
787 outlet glaciers from 1995 to 2013, Cryosphere, 9(3), 957–969, doi:10.5194/tc-9-957-2015,
788 2015.
789 Yang, K. and Smith, L. C.: Supraglacial streams on the Greenland Ice Sheet delineated
790 from combined spectral – shape information in high-resolution satellite imagery, IEEE
791 Geosci. Remote Sens. Lett., 10(4), 801–805, doi:10.1109/LGRS.2012.2224316, 2013.
792
793

794

817
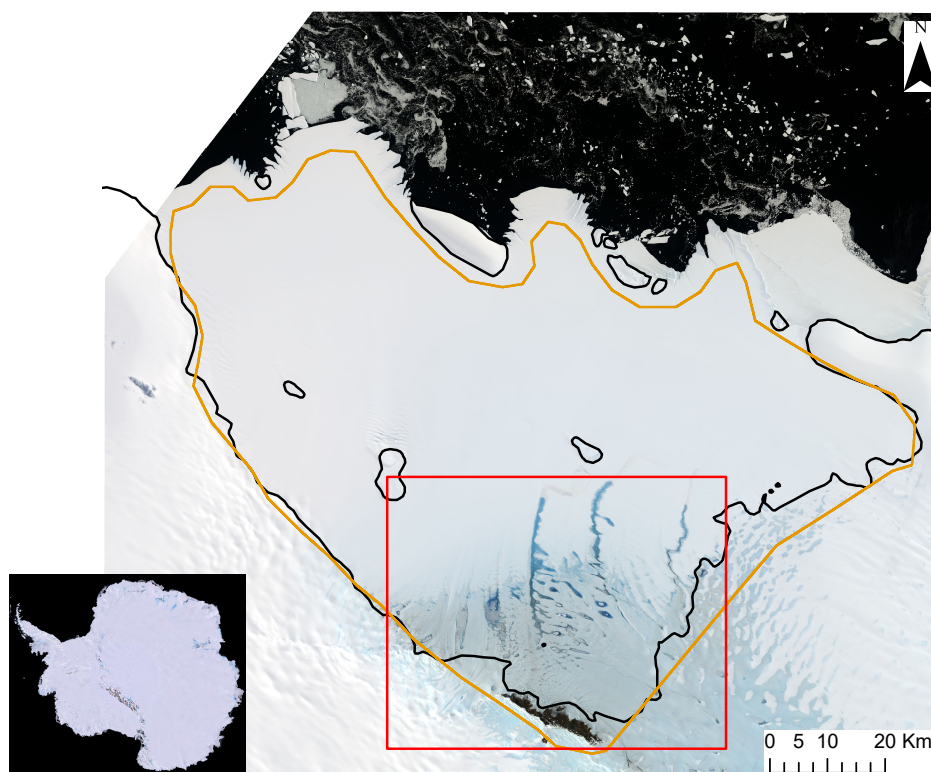
Figure 1: RGB Landsat image of the Nivlisen Ice Shelf acquired on 26th January 2017. The solid black line marks the grounding line, according to the NASA Making Earth System Data Records for Use in Research Environments (MEaSUREs) Antarctic boundaries dataset (Mouginot et al., 2017). The solid orange line shows the study area extent used for this study, and the solid red line marks the area shown in all subsequent figures. The red star on the inset shows the location of the Nivlisen Ice Shelf in the context of an image of Antarctica, which is a mosaic product based on sources from USGS, NASA, National Science Foundation, and the British Antarctic Survey (https://visibleearth.nasa.gov/view.php?id=78 592).

826

827
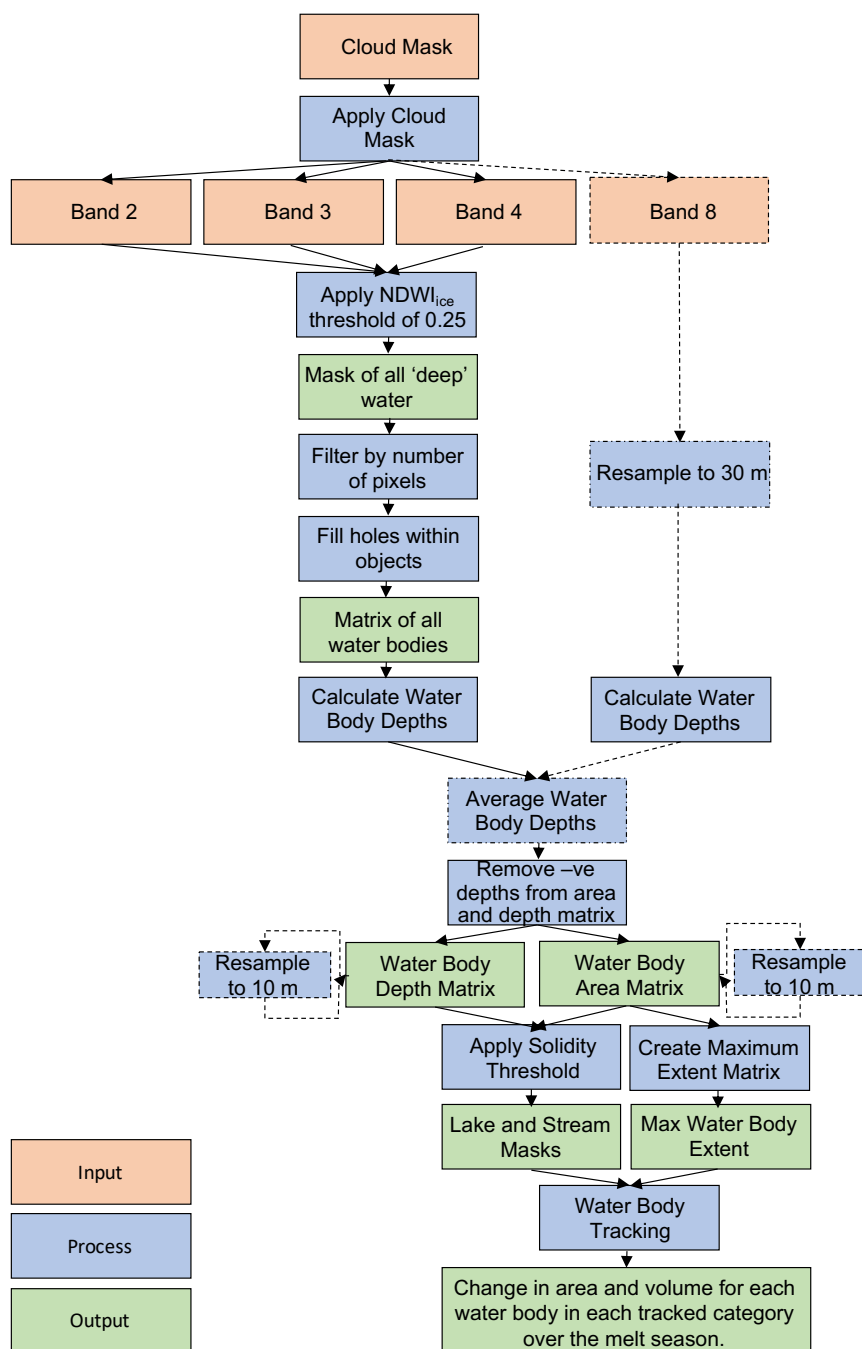
Figure 2: A workflow detailing the methods applied to both the Landsat 8 and Sentinel-2 images through the FASTISh algorithm in MATLAB. Dashed lines indicate steps that were applied to Landsat 8 images only, whereas solid lines indicate steps that were applied to both sets of image types. Modified from Williamson et al. (2018b).
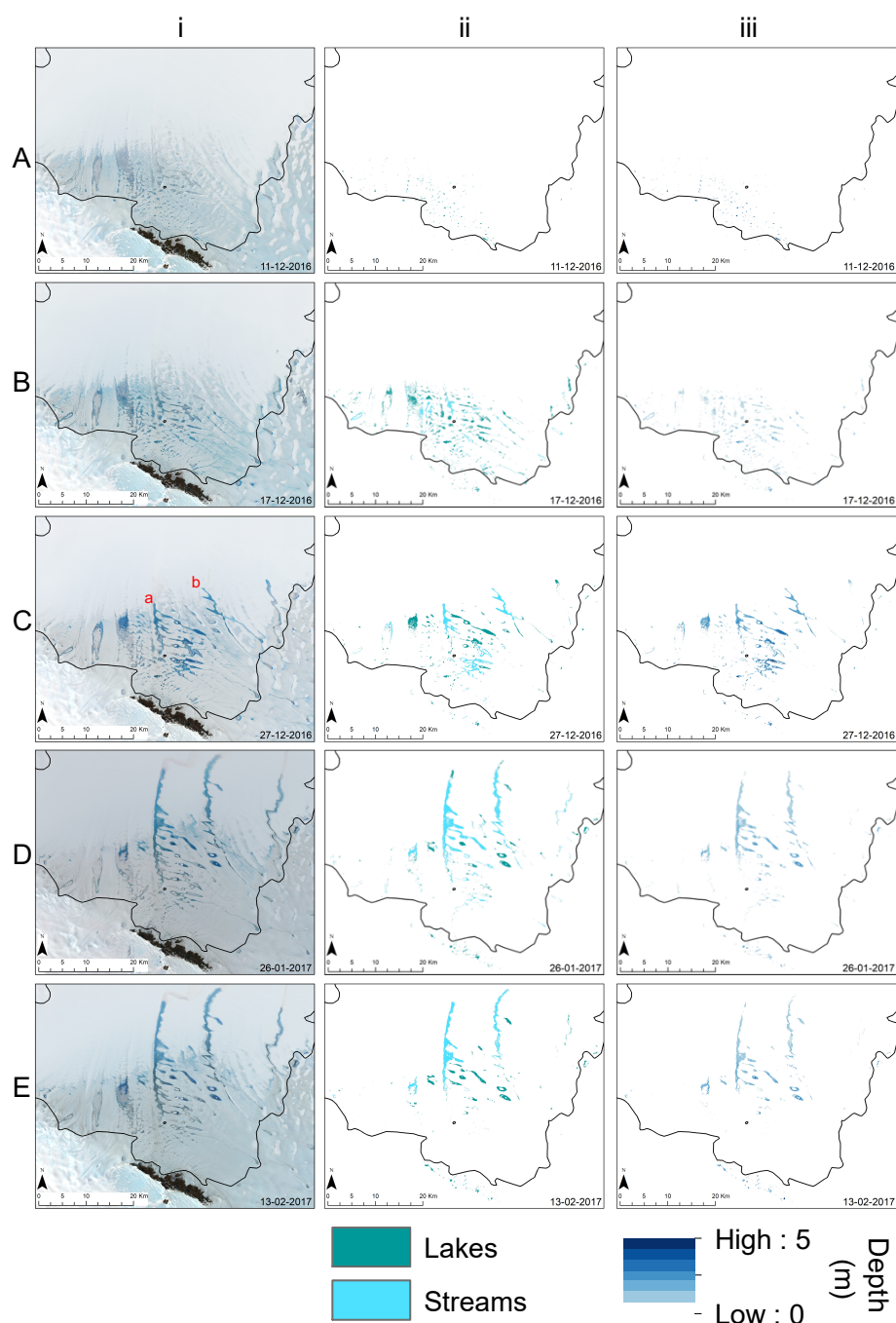
835
836
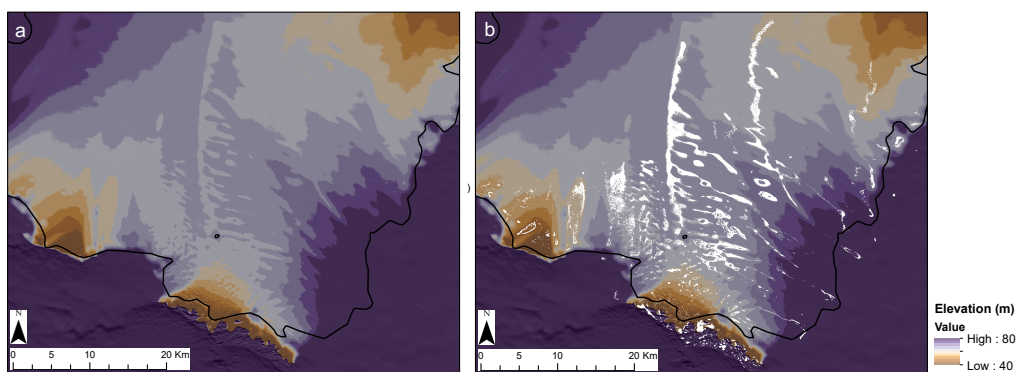
837
838
839 *Figure 3: (a) DEM mosaic of the Nivlisen Ice Shelf, (b) DEM mosaic of the Nivlisen Ice Shelf overlain*
840 *with the maximum extent matrix for the 2016-2017 melt season in white. DEM data sourced from the*
841 *REMA dataset (Howat et al., 2019).*
842
843

Figure 4: Five of the eleven dates studied in the 2016-2017 melt season (represented by labels A-E), and their corresponding (i) RGB images, (ii) lake and stream area masks, (iii) depth masks. See S.1 for all RGB images, S.2 for all lake and stream area masks and S.3 for all depth masks produced in this study.

850
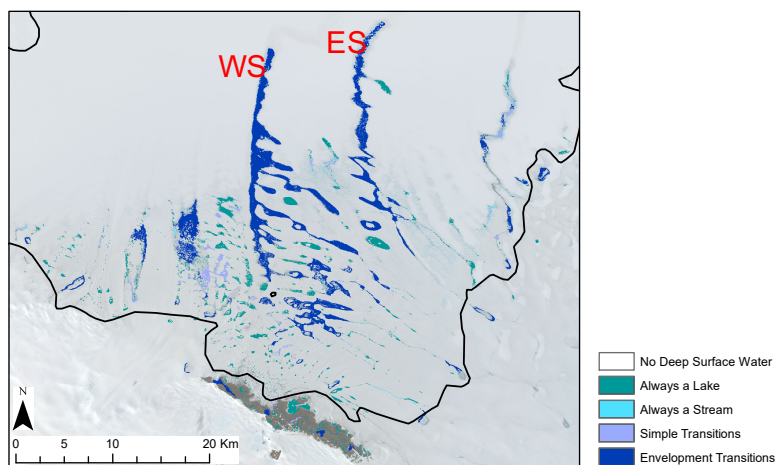
851
852 *Figure 5: The maximum extent of all identified water bodies on the Nivlisen Ice Shelf for the 2016-*
853 *2017 melt season, colour coded by water body type. 'WS' donates 'Western System', and 'ES' is*
854 *Eastern System.*

855
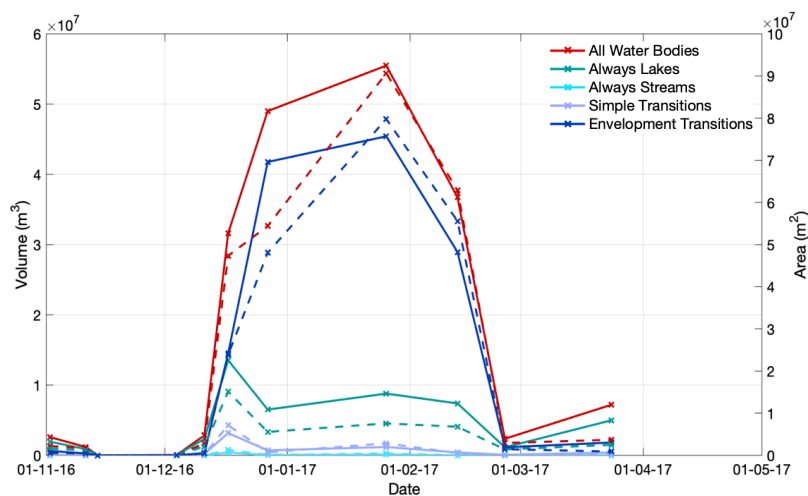
856
857 Figure 6: The total area and volume held in each water body category over the 2016-2017 melt
858 season on the Nivlisen Ice Shelf. Volumes are indicated by the solid lines, and areas by the
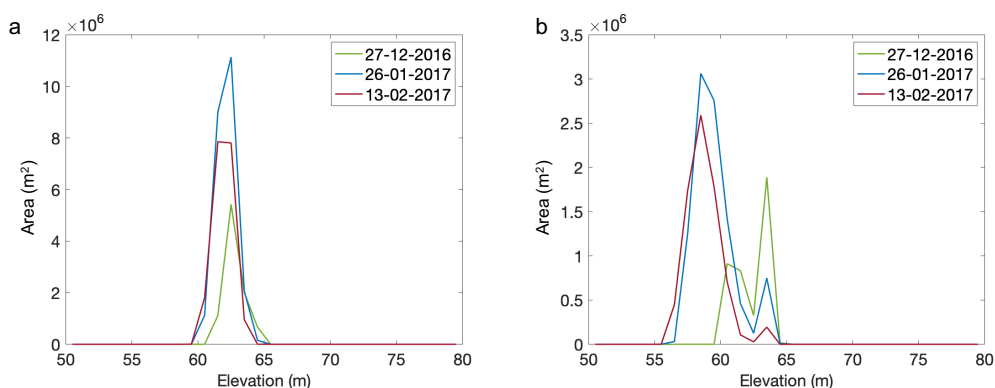859 dashed lines.

860

Figure 7: Elevation Distribution Plots for (a) the Western System (WS) and (b) the Eastern System (ES) on the Nivlisen Ice Shelf for three dates in the melt season. Data points are plotted at the mid-point of their elevation bins along the X axis.
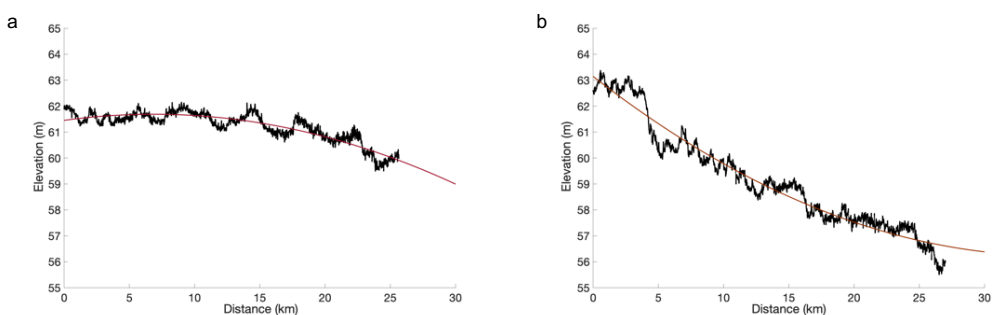

Figure 8: Elevation profiles for (a) the WS and (b) the ES, fitted with quadratic trendlines (in red). These data are extracted from REMA (Howat et al., 2019) and the path of data extraction was guided using the maximum depth matrix of both the WS and ES over the full 2016-2017 melt season (see S.6).
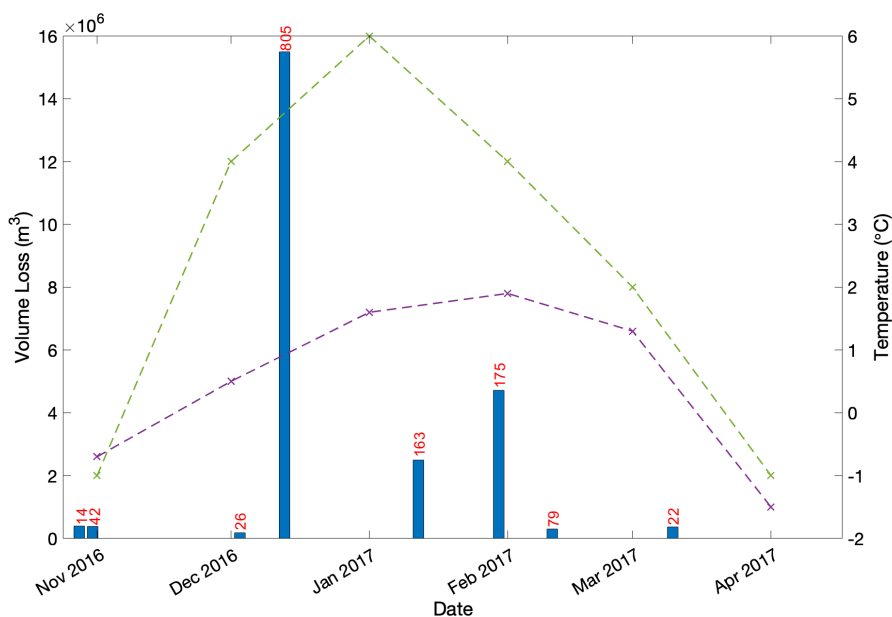
875
876
877 *Figure 9: The total volume lost in 'loss events' from water bodies in the 'always a lake' category,*
878 *plotted as bars. The total number of loss events for each date is indicated above each bar. Ground*
879 *surface temperatures (purple) and air surface temperatures (dashed) are also plotted as dashed*
880 *lines.*

881
882 *Table 1: Maximum Area and Volume and the corresponding dates for each water body category on*
883 *the Nivlisen Ice Shelf in the 2016-2017 melt season.*

	Maximum Volume (m³)	Maximum Area (m²)	Date of Maximum Volume	Date of Maximum Area
All Water Bodies	5.5 x 10⁷	9.1 x 10⁷	26ᵗʰ January 2017	26ᵗʰ January 2017
Always Lakes	1.4 x 10⁷	1.5 x 10⁷	17ᵗʰ December 2016	17ᵗʰ December 2016
Always Streams	3.9 x 10⁵	1.3 x 10⁶	17ᵗʰ December 2016	17ᵗʰ December 2016
Simple Transitions	3.2 x 10⁶	3.2 x 10⁶	17ᵗʰ December 2016	17ᵗʰ December 2016
Envelopment Transitions	4.5 x 10⁷	8.0 x 10⁷	26ᵗʰ January 2017	26ᵗʰ January 2017

884

24